Research Square

Preprints are preliminary reports that have not undergone peer review.
They should not be considered conclusive, used to inform clinical practice,
or referenced by the media as validated information.

Polyaniline-Mediated Dual Z-Scheme Heterostructure Nanocomposite (CeO2–MnSe2–PANI) for Efficient Degradation of Organic Dyes

Nagina Naveed Riaz
University of Education
Muhammad Imran
University of Education
Khalil Ahmad
Emerson University, Multan
Zuha Shahid
University of Education
Muhammad Mahboob Ahmed
Bahauddin Zakariya University
Eman Aldosari
King Saud University
Ahmad Hosseini Bandegharaei
ahoseinib@semnan.ac.ir
Semnan University

Article

Keywords: Nanocomposite, Wastewater remediation, Dual Z-Scheme Heterojunction, Solar-Driven Photocatalysis, CeO2–MnSe2–PANI nanocomposite, Charge Separation

Posted Date: November 26th, 2026

DOI: https://doi.org/10.21203/rs.3.rs-11715047/v1

License: This work is licensed under a Creative Commons Attribution 4.0 International License.
Read Full License

Additional Declarations: No competing interests reported.

Polyaniline-Mediated Dual Z-Scheme Heterostructure Nanocomposite (CeO_2–$MnSe_2$–PANI) for Efficient Degradation of Organic Dyes

Nagina Naveed Riaz [a*], Muhammad Imran [a], Khalil Ahmad [b*], Zuha Shahid[a], Muhammad Mahboob Ahmed [c], Eman Aldosari [d], Ahmad Hosseini Bandegharaei [e*]

[a] Department of Chemistry, Division of Science & Technology, University of Education, 54770 Lahore, Vehari Campus, Pakistan

[b] Department of Chemistry, Emerson University, 60700 Multan, Pakistan

[c] Institute of chemical sciences, Bahauddin Zakariya University, 60800 Multan, Pakistan

[d] Department of Chemistry, College of Science, King Saud University, P. O. Box 2455, Riyadh 11451, Saudi Arabia

[d] Faculty of Chemistry, Semnan University, Semnan, Iran

[e] Scientific Research Centre, Al-Ayen Iraqi University (AUIQ), Nasiriyah, Thi-Qar, 64001, Iraq

[f] Department of Sustainable Engineering, Saveetha School of Engineering, SIMATS, Chennai, Tamil Nadu 602105, India

[a*]*Corresponding Authors: naginanaveed@ue.edu.pk* (N. N. Riaz*), Khalil Ahmad: *khalil.ahmad@eum.edu.pk* Ahmad Hosseini Bandegharaei: *ahoseinib@semnan.ac.ir*

Abstract

Organic dye pollutants discharged by textile, leather, and pharmaceutical industries pose a persistent threat to aquatic ecosystems and human health, necessitating efficient, sustainable remediation strategies. In the present work, a polyaniline-supported dual Z-scheme heterostructure CeO_2–$MnSe_2$–PANI was synthesized via a combined hydrothermal, sol-gel, and oxidative polymerization route for the solar-driven photocatalytic degradation of organic dyes. XRD confirmed the phase purity of the binary and ternary nanocomposites, while TEM and HRTEM verified the intimate interfacial contact and stacking of CeO_2, $MnSe_2$, and PANI within the ternary heterostructure. The ternary nanocomposite exhibited a narrow optical band gap of 2.66 eV and achieved a maximum degradation efficiency of 99.85% against methylene blue under sunlight irradiation, with a rate constant of 0.074 min^{-1} substantially outperforming pristine CeO_2, $MnSe_2$, and the binary CeO_2–$MnSe_2$ composite. Optimal photocatalytic performance was obtained at 1 mg catalyst loading, pH 8, and 10 ppm dye concentration. The

results of radical trapping experiments revealed that $^{\bullet}O_2^-$ and $^{\bullet}OH$ were the primary active species during the photodegradation process. Additionally, the photocatalyst exhibited excellent structural stability and reusability over multiple photocatalytic cycles. Consequently, the designed polyaniline supported dual Z-scheme heterostructure demonstrates significant potential as a robust, scalable photocatalyst for advanced wastewater remediation.

Keywords: *Nanocomposite, Wastewater remediation; Dual Z-Scheme Heterojunction; Solar-Driven Photocatalysis; CeO_2–$MnSe_2$–PANI nanocomposite; Charge Separation*

1. Introduction

These days, many rapidly growing industries, such as printing, leather, cosmetics, food, textiles, medical labs, and pharmaceuticals, release large amounts of organic dyes into clean water sources, polluting drinking water day by day [1]. Many industries use harmful, carcinogenic dyes without regard for the ecological environment and human health [2]. These dyes persist in water without breaking down, posing serious risks to aquatic life. Consequently, it is very important to mitigate these water pollution problems using sustainable, efficient water remediation techniques, as conventional methods such as biological treatment, sedimentation, adsorption, coagulation, and chemical processes are readily available [3]. However, these techniques usually merely transform these dye pollutants into other forms of pollutants during wastewater treatment, thereby incurring high costs and energy requirements [4]. Solar-driven semiconductor photocatalysis is among the most effective methods for degrading dye pollutants. Semiconductor photocatalysis uses sunlight to create chemical reactions that break down the structure of pollutants. This approach works efficiently, does not produce secondary pollutants, is low-cost, and consumes less energy [5,6]. Photo-decomposition of dye pollutants begins when light with energy equal to or greater than the target material's band gap ($h\nu \geq Eg$) strikes the material. This light energy creates electron–hole pairs, which then start the reaction [7]. Upon photoexcitation, the photogenerated holes produced in the valence band (VB) and

electrons produced in the conduction band (CB) of a target material cause the formation of reactive oxygen species (oxide radicals/hydroxyl radicals), which then break the dye structure and produce harmless species (CO_2, H_2O and Mineral Acids) [8]. Most inorganic photocatalysts have a narrow spectral absorption range and are inefficient in visible light, which limits their practical use [9]. Therefore, designing efficient solar light-mediated photocatalysts has become an active area of research.

In recent years, nanostructured metal oxides have attracted significant attention as catalysts for photocatalytic applications [10,11]. Among a wide range of metal oxides, rare-earth n-type cerium dioxide (CeO_2) has attracted significant interest as a photocatalyst due to its high photocatalytic efficiency, thermal and chemical stability, cost-effectiveness, resistance to photo-corrosion, and environmentally friendly properties [12-14]. Nevertheless, some issues are associated with cerium dioxide (CeO_2), particularly its wide band gap (approximately 3.2 eV), which limits its absorption to high-energy photons in the ultraviolet (UV) region, thereby limiting its further application in the visible light spectrum. Additionally, the fast recombination rate of $e^-/h+$ pairs in CeO_2 prevents it from being an ideal photocatalyst for water treatment [15]. Hence, there is a need to stimulate its photodegradation ability to overcome the above shortcomings.

To fully utilize visible light and to improve the recombination rate of e^-/h^+, various methods, such as doping [16], dual doping [17], noble metal incorporation [18], and composite formation [19,20] have been established. From all of these methods, the best strategy is the coupling of CeO_2 with another semiconductor, forming a composite, such as Cu_2O/CeO_2 [21], $NiFe_2O_4/CeO_2$ [19], Ag_3PO_4/CeO_2 [22] and $BiVO_4/CeO_2$ [23], which have shown high efficiency in the photo-decomposition of organic dyes. Unfortunately, the formation of such a conventional heterojunction between two semiconductors decreases the reducing and oxidizing capabilities of electrons and holes because, in this case, electrons and protons with high

reducing and oxidizing potentials move toward the lower reducing and oxidizing potentials of the other semiconductor, and their redox capabilities decrease.

In contrast to conventional heterojunctions, Z-Scheme heterojunction photocatalysis, such as g-C_3N_4/CeO_2 [24] and α-Fe_2O_3/CeO_2 [25], the photogenerated electrons in the conduction band of CeO_2, having a weak reduction potential, recombine with weak oxidation potential photogenerated holes in the valence band of other materials (e.g., g-C_3N_4 and α-Fe_2O_3) [26]. In this way, the recombination of weak reducing power electrons and weak oxidizing power holes resulted in the retention of highly oxidizing power holes in the valence band of CeO_2 and highly reducing power electrons in the conduction band of the coupled material. This system provides an effective approach to addressing the limitations of conventional heterojunction photocatalytic systems.

Notably, constructing a Z-scheme heterojunction for charge-carrier movement by coupling CeO_2 with a material having a low band gap represents an effective strategy to control the rapid recombination of charge carriers, thereby improving charge separation, enhancing redox ability, and improving visible-light absorption [27]. Nevertheless, selecting a suitable coupling material with a small band gap for a Z-scheme construction remains a significant challenge. As metal selenides are small band gap semiconductors and their application as photocatalysts for the dye degradation have been studied [28-30], so, during the investigation of a small band gap material suitable for constructing a z-scheme with CeO_2, environmentally friendly and low cost manganese diselenide ($MnSe_2$) is stand out as promising option because of its small band gap of about 2eV [31], ability to absorb visible light and well aligned band positions with CeO_2 make it an ideal candidate to form an efficient Z-scheme heterojunction with CeO_2. Manganese often stabilizes in mixed-valence compounds, simultaneously occupying trivalent (+3) and tetravalent (+4) oxidation states within the crystal structure. In $MnSe_2$, the Mn^{4+} cation is octahedrally coordinated to six equivalent Se^{2-} ions, forming the cubic $MnSe_2$ lattice.

Manganese's strong magnetism from its 3d electrons forces the sp electrons/holes of Se to align their spins. This powerful magnetic control over charge carriers gives $MnSe_2$ special magnetic, optical, and ferromagnetic properties [32]. However, the binary CeO_2-$MnSe_2$ Z-scheme heterojunction suffers from slow charge transfer at the interface of these two semiconductors, which limits the overall photocatalytic performance of this system. To circumvent this shortcoming, an electron mediator, such as Polyaniline (PANI), is introduced into this system [33].

Polyaniline is a highly conductive semiconductor polymer known for its stability and low cost [34,35], making polyaniline (PANI) one of the best electron mediators for charge transfer at the interface between two semiconductors in a Z-scheme heterojunction. Surprisingly, besides working as an electrode mediator, PANI can also function as a photocatalyst and participate directly in photocatalytic reactions in a semiconductor heterojunction photocatalytic system [36-38], to form a dual Z-scheme CeO_2-$MnSe_2$-PANI heterojunction with improved charge separation and rapid interfacial charge transfer. Polyaniline (PANI) is a promising photocatalytic material owing to its distinctive electrical conductivity, facile synthesis, and robust chemical stability [39]. The delocalized π–π conjugated structure and narrow band gap (about 2.7 eV) of PANI improve the fraction of visible light utilization [40]. Several studies have reported the use of polyaniline (PANI) as a photocatalyst in dual Z-scheme heterojunctions such as PANI/Sb_2S_3/ZnO [41], PANI/Ag_3PO_4/CNO [33], Ag_2CO_3/Ag/PANI [42] and PANI/Ag_2O/Cu_2O [43].

Herein, a polyaniline (PANI) supported dual Z-scheme heterostructure ternary nanocomposite CeO_2-$MnSe_2$-PANI was successfully synthesized via a combination of hydrothermal, sol-gel and simple oxidative polymerization methods (as shown in Scheme 1), along with binary composite CeO_2-$MnSe_2$ and individual components CeO_2 and $MnSe_2$ and their physical properties were systematically examined using multiple analytical techniques. The

photocatalytic performances of CeO_2, $MnSe_2$, CeO_2-$MnSe_2$ and CeO_2-$MnSe_2$-PANI were assessed by decomposing methylene blue (MB) dye. In this work, various influencing factors, including catalyst dosage, dye concentration, and pH, are also studied in detail. The photodegradation mechanism of CeO_2-$MnSe_2$-PANI was also proposed (as shown in Scheme 2) and elaborated on the basis of reactive species trapping experiments. The recyclability of the CeO_2–$MnSe_2$–PANI photocatalyst was evaluated through repeated degradation cycles to assess its stability and reusability. To the best of my knowledge and based on the available literature, this study is the first to report on the synthesis of a polyaniline-supported dual Z-scheme ternary nanocomposite, CeO_2–$MnSe_2$–PANI, for photocatalytic dye degradation.

2. Experimental Approach

2.1. Reagents

Sodium borohydride ($NaBH_4$), Manganese chloride tetrahydrate ($MnCl_2.4H_2O$), Ammonium persulfate, Cerium nitrate hexahydrate ($Ce(NO_3)_3.6H_2O$, Aniline, Selenium powder, Ammonia solution (NH_4OH), Hydrochloric acid (HCl), Ethanol (EtOH) and Deionized water. All reagents were sourced from Sigma-Aldrich and used as supplied, with no additional purification.

2.2. Synthesis of $MnSe_2$

$MnSe_2$ was synthesized through a hydrothermal route. At first, equal amounts (0.5 g) of selenium powder and manganese chloride tetrahydrate ($MnCl_2.4H_2O$) were dissolved in 50 mL of an ethanol/water solution. To this solution, ultrasonic stirring was applied for 1 hour, after which a 0.1 M aqueous solution of $NaBH_4$ was added dropwise. The resulting solution was stirred ultrasonically for another hour to form a homogeneous mixture. Thereafter, a beaker containing this homogeneous solution was treated hydrothermally in a stainless steel autoclave at 200˚C. Following a complete hydrothermal reaction of 9 hours, the autoclave was cooled to room temperature. The resulting powder was collected and centrifuged. To remove any

remaining impurities, the collected powder was washed repeatedly with deionized water and subsequently dried in an oven at 80 °C for 10 hours. The final bulk $MnSe_2$ product was obtained and finely ground for physical and photocatalytic characterization.

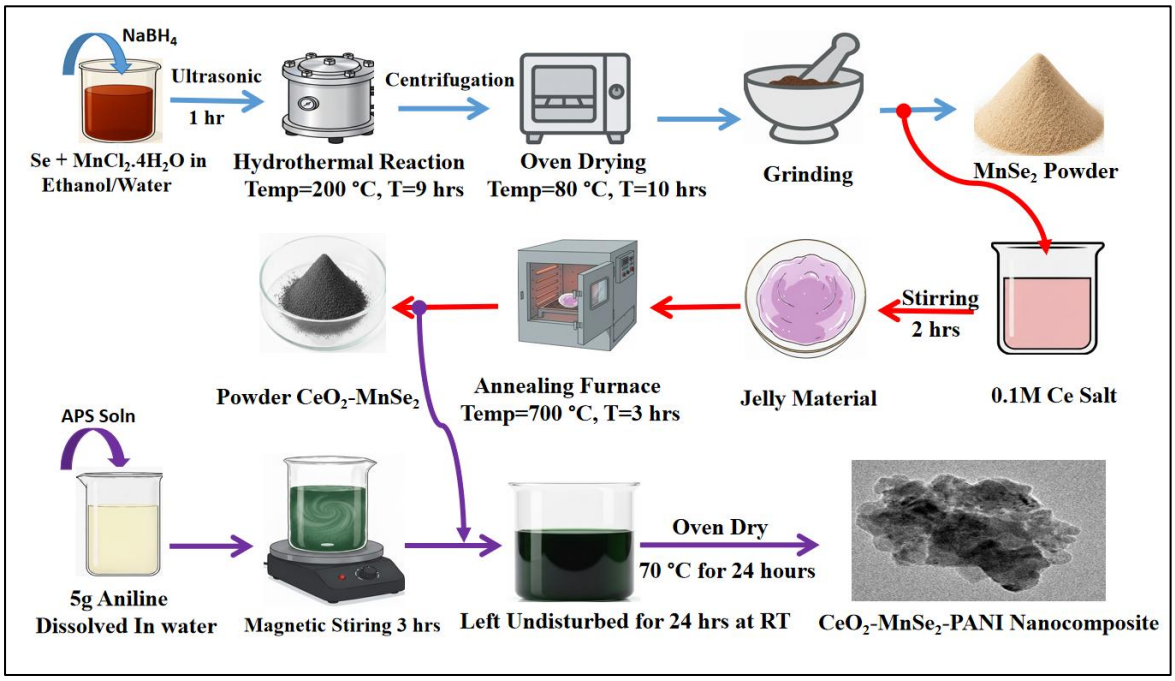
2.3. Synthesis of CeO_2-$MnSe_2$ and pure CeO_2

A facile sol-gel method was used to synthesize CeO_2-$MnSe_2$. For the preparation of CeO_2-$MnSe_2$, cerium nitrate hexahydrate ($Ce(NO_3)_3 \cdot 6H2O$) was used as a precursor. At first, 0.1 M solution of cerium salt was prepared in deionized water and continuously stirred on a hot plate at 70 °C to achieve complete dissolution. Moreover, the aqueous ammonia was slowly trickled into the solution to achieve a final pH of about 9. Furthermore, 0.2 g of as-prepared $MnSe_2$ was added and the resultant suspension was allowed to be magnetically stirred for 2 hours at ~70 ˚C to transform solution into a gel. The obtained gel was dried at 100˚C in an oven and annealed at 700˚C in a furnace for 3 hours to get a fine ground powder. The pure CeO_2 was also synthesized following the same method in the absence $MnSe_2$ particles.

2.4. Synthesis of CeO_2-$MnSe_2$-PANI nanocomposite

A simple oxidative polymerization method was employed to prepare the ternary CeO_2-$MnSe_2$-PANI nanocomposite. Initially, a solution of 5g aniline in 200 ml deionized water was prepared, and its pH was maintained at ~1 via dropwise addition of HCl. In a separate step, 6.125 g ammonium persulfate was dissolved in 100 ml of deionized water to prepare an APS solution. Aniline polymerization was initiated by the continuous dropwise addition of APS solution to the aniline solution for 30 minutes. After magnetically stirring the solution was for 3 hours to ensure homogeneity, 0.5 g of as prepared CeO_2-$MnSe_2$ particles was added to that homogeneous solution. Thereafter, the solution was allowed to stand at room temperature for 24 hours to ensure complete polymerization and the resultant powder was treated with centrifugation. The resultant powder was washed several times using deionized water and dried

in an oven at 70 ˚C for 24 hours. On the following day, the required ternary composite was obtained ground to produce a fine powder.



Scheme 1. Schematic overview of the stepwise synthesis of CeO_2-$MnSe_2$-PANI nanocomposite.

2.5. Photocatalytic Testing Procedure

The photocatalytic degradation studies were conducted under natural sunlight irradiation using methylene blue (MB) as a model organic dye pollutant to assess the photocatalytic performance of the synthesized photocatalysts. Four separate photocatalytic systems were examined using four identical MB solutions, each treated with a different photocatalyst: 1) CeO_2, 2) $MnSe_2$, 3) CeO_2–$MnSe_2$ binary heterostructure composite, and 4) dual z-scheme CeO_2–$MnSe_2$–PANI heterostructure ternary nanocomposite. Four aqueous solutions of MB (10 mg L^{-1}, 50 mL) were freshly prepared using deionized water in four separate quartz beakers and 20 mg of the respective photocatalysts (CeO_2, $MnSe_2$, CeO_2–$MnSe_2$ or CeO_2–$MnSe_2$–PANI) were introduced into them. To establish adsorption-desorption equilibrium between the dye molecules and the surface of photocatalysts before natural sunlight irradiation, these solutions containing photocatalysts were magnetically stirred in the dark environment for 20 minutes at

room temperature. During this process, to ensure dark conditions, these 4 mixtures were protected from light exposure by a tight application of aluminium foil. The photocatalytic reactions were conducted under direct natural sunlight on cloud free days between 11:00 am and 2:00 pm PST, during which solar intensity remains relatively stable. All four reaction beakers were exposed to sunlight simultaneously to ensure identical irradiation conditions. Continuous magnetic stirring was maintained throughout the experiment to achieve uniform dispersion of the photocatalysts and to minimize mass-transfer limitations. During irradiation, 3 mL aliquots were taken out from each reaction mixture at fixed time intervals (every 10 min) and subjected to centrifugation at 5000 rpm for 5 min to remove photocatalysts particles. Then, the resulting supernate was filtered using a 0.22 μm Nylon syringe filter. UV-Vis Spectro-photometry was employed to analyze the final filtered liquid at room temperature by measuring the absorbance of the liquid samples, targeting the specific absorption wavelength of methylene blue (MB) at 663 nm. Based on the Beer-Lambert law [44], the concentration of a light absorbing specie can be determined from its absorbance as these two are directly proportional to each other over a certain concentration range. For comparison, a blank controlled experiment in the absense of photocatalyst was also conducted under identical light irradiation conditions. The efficiency of the photocatalyst was during the degradation process was calculated according to the following equation [45]:

$$Degradation\ (\%) = \left(\frac{C_\circ - C_t}{C_\circ}\right) \times 100 \quad (1)$$

Where, C_0 = Initial dye concentration in dark and C_t = Concentration after a time t. For controlled experiment without a catalyst, C_0 corresponds to the initial concentration of dye in the dark environment, while C_t is the dye concentration after a given time period under sunlight exposure. To determine the photocatalytic reaction rates of the photocatalysts, pseudo-1st-order kinetic equation was applied which is based on the comparison of initial concentration

of dye in the dark and final concentration of dye after a specific time period of sunlight exposure [46]**:**

$$ln \frac{C_o}{C_t} = kt \quad (2)$$

where, k = apparent rate constant and t = exposure time. All photocatalytic experiments were performed under identical experimental conditions to ensure reproducibility and accurate comparison among the four MB samples.

Additionally, the durability and reusability of the synthesized ternary photocatalyst was assessed over six consecutive photocatalytic cycles. The effects of key factors such as initial dye concentration, catalyst loading, and pH variations were also investigated to assess their impact on the degradation efficiency. Furthermore, active species trapping experiments were performed under the same light conditions to identify the predominant reactive species using some selective scavengers.

2.4. Analytical Characterization Tools

A comprehensive characterization was performed to investigate the optical, structural, and morphological properties of the synthesized dual Z-scheme photocatalyst using multiple analytical characterization techniques. Crystalline phase determination was carried out via X-ray diffraction (XRD) technique using an XRD instrument (Bruker-D8) with a Cu-Kα radiation source (λ = 1.5406 Å). A Pen-type pH meter (HI 98103, HANNA) was used to measure the pH value of dye solutions. The light-harvesting efficiency and optical absorption properties of both binary and ternary nanocomposites were examined by UV–visible spectroscopy (Carry-60 Agilent) across a wavelength range of 200–800 nm, and the band gaps were estimated accordingly. While, transmission electron microscopy (TEM) analysis was conducted using a transmission electron microscope (JEOL JEM-2100FS) to elucidate the microstructural features and interfacial contact between the coupled components, providing clear evidence for the successful formation of the dual Z-scheme heterojunction.

3. Results and Discussion

3.1. XRD

To investigate the crystallinity structure and phase purity of already synthesized binary CeO_2-$MnSe_2$ and ternary CeO_2-$MnSe_2$-PANI nanocomposites, XRD analysis was performed and the resulting patterns are shown in Fig. 1. The diffraction peaks marked with blue diamonds correspond to the (111), (200), (220), (222), and (420) planes. These match the cubic fluorite structure of CeO_2 (JCPDS card no-01-081-0792). While the diffraction peaks marked with red stars coincide with (111), (200), (211), (221), (023), (321), and (331) that represent cubic phase structure of $MnSe_2$ (JCPDS card no-03-065-3336). Both samples show well defined, sharp peaks, indicating high crystallinity. It is clear that the positions of both binary and ternary samples peaks remain consistent. In the ternary CeO_2-$MnSe_2$-PANI pattern, there is no distinct sharp peak for Polyaniline which is typically attributed to the amorphous nature of PANI. No other impurity related diffraction peak was present beyond those of CeO_2 and $MnSe_2$ in the XRD spectra, which verified the successful formation and phase integrity of polyaniline supported CeO_2–$MnSe_2$–PANI ternary nanocomposite.

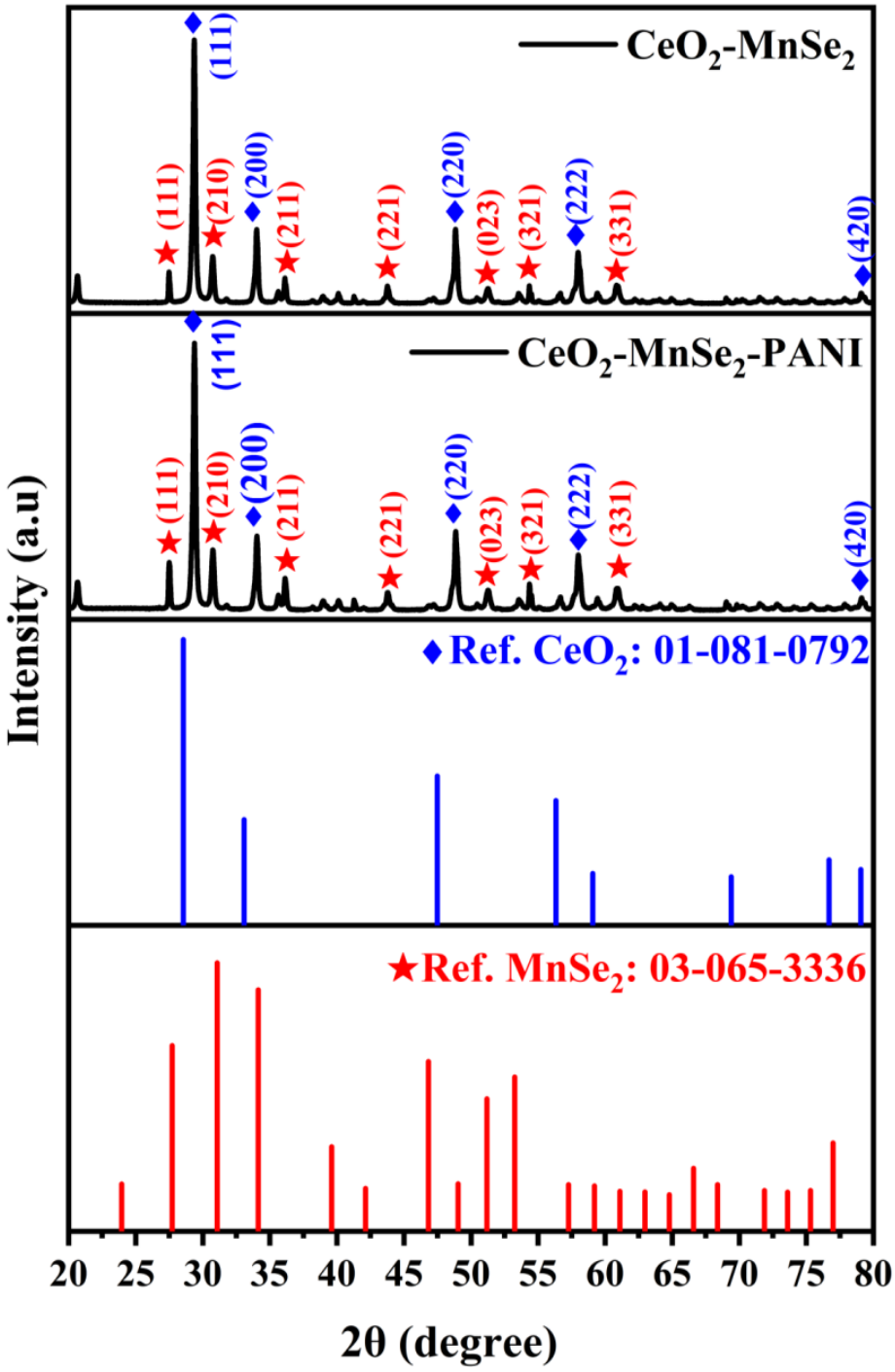


Fig. 1. XRD spectrum of binary (CeO_2-$MnSe_2$) and ternary (CeO_2-$MnSe_2$-PANI) nanocomposites compared with standard data.

3.2. UV-Visible Spectroscopy

The optical behaviors of both synthesized binary CeO_2-$MnSe_2$ and ternary CeO_2-$MnSe_2$-PANI nanocomposites were investigated via UV–visible spectroscopy. The light absorption

capability and band gap energy are important factors that decide the photo catalytic capability of a photocatalyst. As shown in Fig. 2.(a), both CeO_2–$MnSe_2$ and CeO_2–$MnSe_2$–PANI nanocomposites showed a highly efficient absorption in the UV spectrum, which gradually extends into the visible region. Notably, the ternary CeO_2–$MnSe_2$–PANI nanocomposite showed significantly greater light absorption in the visible range compared to binary CeO_2–$MnSe_2$ nanocomposite, indicating improved visible light harvesting capability due to the synergistic coupling of PANI. Such an improved visible light absorption in ternary nanocomposite can be assigned to the π–π* transitions alongside the conductive nature of PANI, which facilitates better photon absorption.

In addition, optical band gap energies (E_g) of both CeO_2-$MnSe_2$ and CeO_2-$MnSe_2$-PANI nanocomposites were determined using the Tauc plot method assuming an indirect transition (n= 1/2). The corresponding graph, plotting $(\alpha hv)^2$ as a function of photon energy, is shown in Fig. 2(b). The optical band gap energies were calculated using the fundamental Tauq relation given as [47]:

$$(\alpha hv)^{1/n} = A(hv - E_g) \quad (3)$$

Where α represents the absorption coefficient, hv denotes the photon energy, A signifies the proportionality constant, and E_g is the optical band gap energy. To estimate the optical band gap energy (E_g), a tangent was drawn along the linear region of the Tauc plot down to touch the x-intercept on the photon energy x-axis. The calculated E_g values were 2.89 eV and 2.66 eV for CeO_2-$MnSe_2$ and CeO_2-$MnSe_2$-PANI respectively. The narrow band gap of CeO_2-$MnSe_2$-PANI photocatalyst enables efficient absorption of visible light, enhancing its photocatalytic performance.

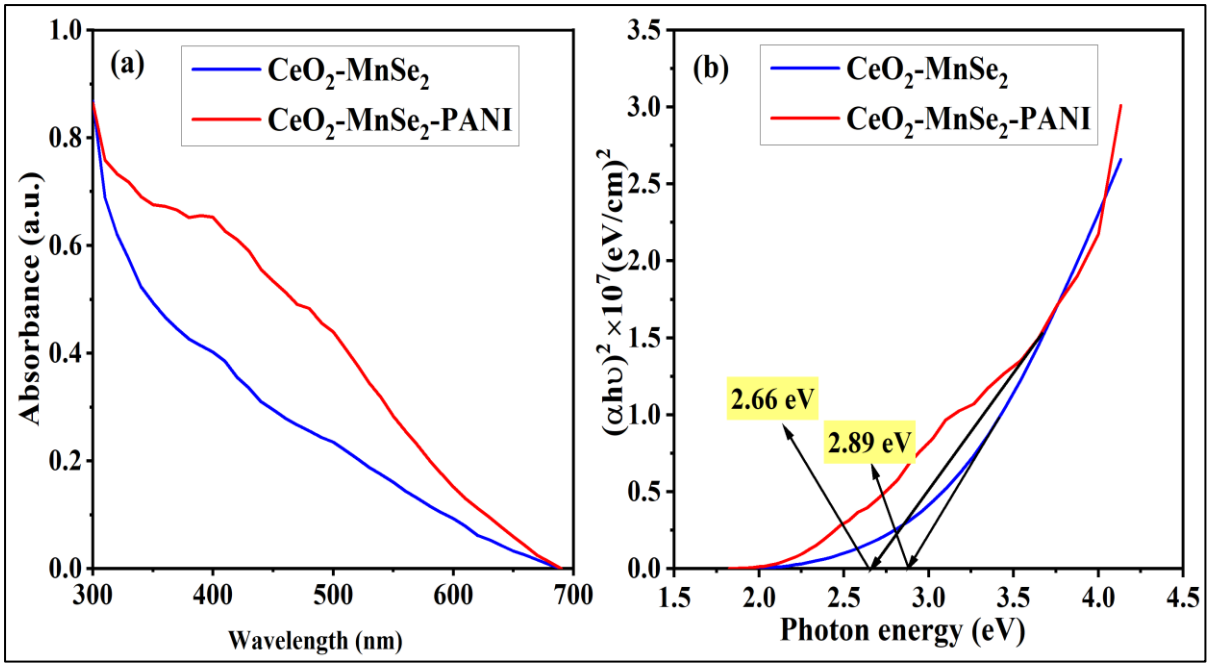


Fig. 2. (a) UV-Vis absorption spectra of binary CeO_2-$MnSe_2$ and ternary CeO_2-$MnSe_2$-PANI nanocomposites and (b) Tauc's plots of binary CeO_2-$MnSe_2$ and ternary CeO_2-$MnSe_2$-PANI nanocomposites for band gap calculations.

3.3. TEM

The microstructure of polyaniline supported CeO_2–$MnSe_2$–PANI nanocomposite was investigated through TEM and HRTEM images at 200 nm, 50 nm, and 5nm as shown in Fig. 3(a, b and c). The TEM micrographs have revealed a well-defined hierarchical hybrid structure. The TEM image recorded at 200 nm scale (Fig. 3a) showed that the composite appeared as irregularly shaped agglomerated nanoclusters where inorganic nanoparticles CeO_2 and $MnSe_2$ are effectively embedded within a photoactive polymer matrix PANI. Upon closer inspection at 50 nm magnification (Fig. 3b), distinct contrast variations are clearly observed, confirming the co-existence of different phases within the CeO_2–$MnSe_2$–PANI nanocomposite. The darkest contrast regions corresponded to CeO_2 nanoparticles due to higher atomic number of cerium which results in strong electron scattering. While on the other hand, relatively lighter dark regions are attributed to $MnSe_2$ nanoparticles. The CeO_2 nanoparticles are anchored onto the relatively larger and more structured domains of $MnSe_2$ nanoparticles. A crucial

observation is the presence of thin, translucent and amorphous layer surrounding the whole inorganic assembly consisting of CeO_2 and $MnSe_2$ nanoparticles. The fuzzy grey contrast area at the edges of the clusters corresponds to the polyaniline coating, establishing a continuous conductive pathway for charge carriers between CeO_2 and $MnSe_2$, which is essential for enhancing photocatalytic activity. The HRTEM image (Fig. 3c) provides clear lattice fringes, confirming the crystalline nature of CeO_2–$MnSe_2$–PANI nanocomposite. Two distinct interplanar spacings were measured using ImageJ software from which (1) d=0.276 nm, owing to the (200) plane of cubic CeO_2, and (2) d=0.205 nm, assigned to the (220) plane of $MnSe_2$ [14]. The simultaneous presence of these well-resolved lattice fringes within a single region strongly confirms the intimate interfacial contact between CeO_2 and $MnSe_2$. No additional impurity-related lattice spacings were observed, indicating high phase purity.

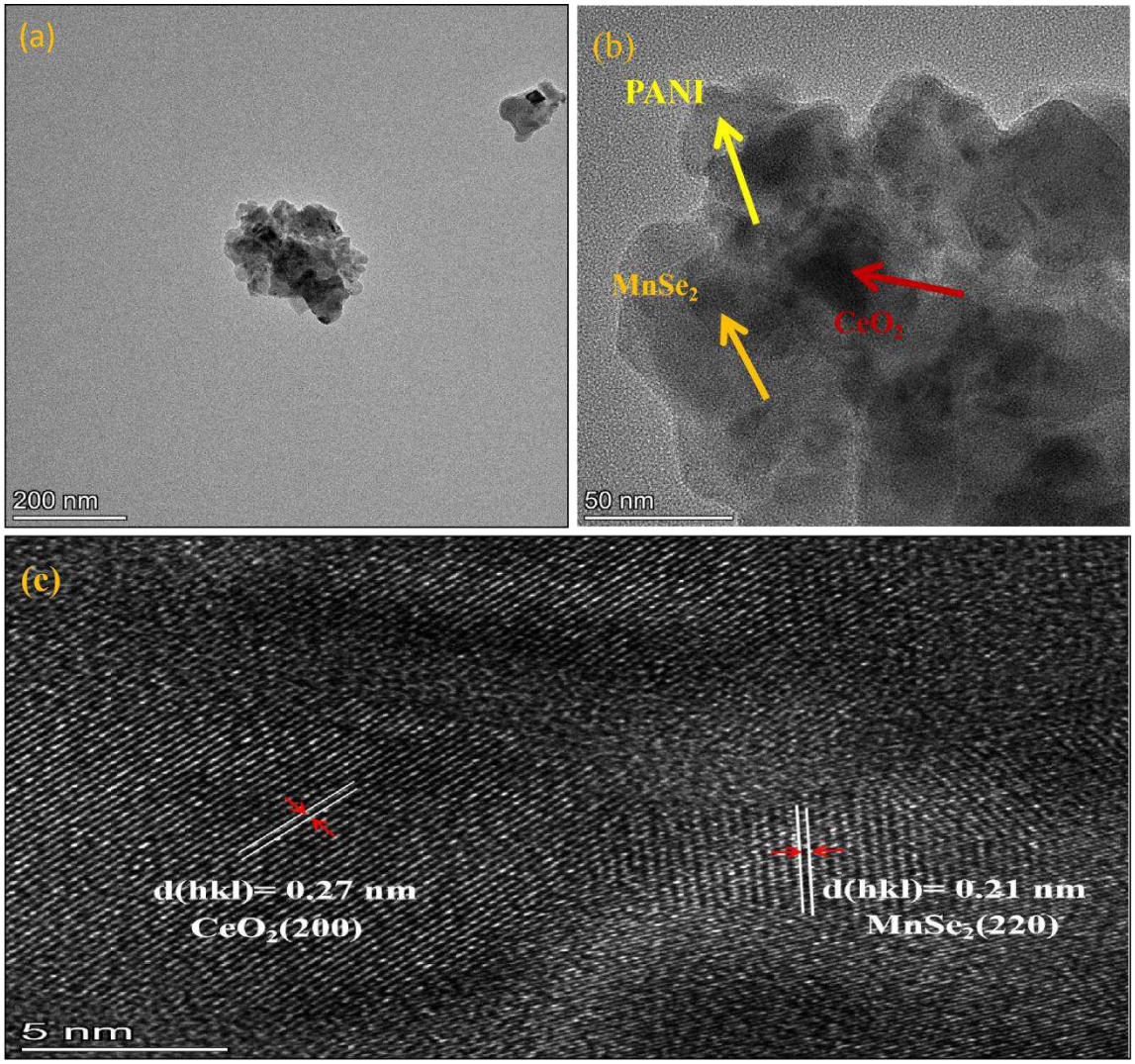


Fig. 3. TEM and HRTEM Analysis of CeO_2–$MnSe_2$–PANI Nanocomposite (a) Low resolution TEM image at 200 nm, (b) Detailed microstructural view by at 50 nm, and (c) HRTEM Image at 5 nm resolution revealing lattice fringes with interplanar spacings of 0.27 nm and 0.21 nm, ascribed to the (200) Plane of CeO_2 and (220) Plane of $MnSe_2$ respectively.

3.4. Photocatalytic Activity

The photocatalytic performance of the synthesized photocatalysts was evaluated through the degradation of methylene blue (MB) dye under sunlight irradiation. When irradiated with sunlight, among the tested materials, the polyaniline supported dual z-scheme heterostructure CeO_2-$MnSe_2$-PANI photocatalyst delivered the highest degradation efficiency of 99.85% owing to effective charge separation and fast inter-face charge transfer between the semi-

conductors due to the presence of π-conjugated system in polyaniline. The other photocatalysts such as CeO_2, $MnSe_2$ and CeO_2-$MnSe_2$ showed degradation efficiencies of 49.27%, 77.94%, and 90.93% respectively (as shown in Fig. 4e). The blank MB solution showed almost no degradation under photocatalyst free conditions. The degradation rates of the photocatalysts were calculated through pseudo-first-order kinetic model [46], and k_{app} values against each photocatalyst were calculated using kinetic fitting curves [$\ln(C_o/C_t)$ versus time (t)] (as shown in Fig. 4f). Among the investigated photocatalysts, the polyaniline supported dual z-scheme heterostructure CeO_2-$MnSe_2$-PANI has the largest k_{app} value of 0.074 min^{-1}. The rate constant k_{app} values were 0.0082 min^{-1}, 0.0192 min^{-1}, and 0.0297 min^{-1} for the photocatalysts CeO_2, $MnSe_2$, and CeO_2-$MnSe_2$ respectively.

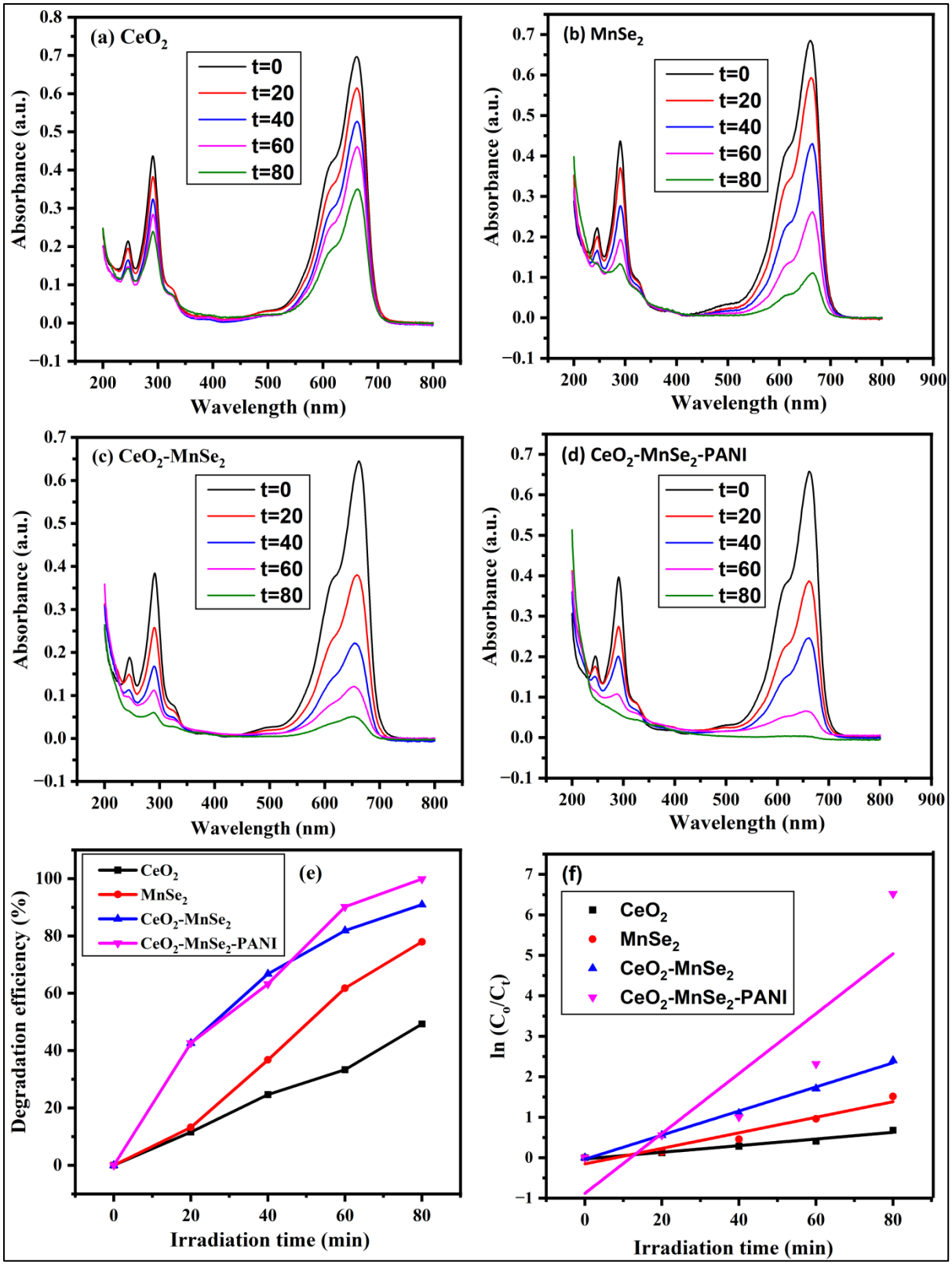


Fig. 4. Variation in absorption with wavelength for degradation of MB dye using: (a) CeO_2, (b) $MnSe_2$, (c) CeO_2-$MnSe_2$, (d) CeO_2-$MnSe_2$-PANI, (e) comparison of time dependent

photodegradation efficiency of different photocatalysts evaluated at regular time intervals, and (f) kinetic plots for different photocatalysts.

The overall results showed that the polyaniline-supported dual z-scheme heterostructure CeO_2-$MnSe_2$-PANI photocatalyst had the best photodegradation ability for the dye pollutants.

3.4.1 Effect of Catalyst Dosage

The effect of catalyst dosage on the photocatalytic degradation of methylene blue (MB) was assessed under sunlight irradiation by varying the amount of polyaniline-supported CeO_2–$MnSe_2$–PANI photocatalyst from 0.5 mg to 3 mg. An increase in catalyst amount led to greater degradation efficiency up to an optimum value. A catalyst dosage of 1 mg proved to be an optimal quantity for the photodegradation of MB, resulting in the highest observed degradation efficiency of 99.81%. Furthermore, the degradation efficiencies of 98.29%, 97.95%, and 95.76% were observed at 0.5 mg, 2 mg, and 3 mg catalyst dosage respectively. The lower degradation efficiency was observed at low catalyst dosages due to the limited availability of active surface sites of catalyst which restricted the formation of reactive oxygen species, thereby lowering the degradation efficiency. Conversely, increasing the catalyst dosage enhanced the number of exposed active sites on the photocatalyst surface and promoted greater light absorption, leading to the formation of more photogenerated charge carriers and reactive species, thereby improving the degradation rate of MB [48]. However, beyond the optimum dosage, a further increase in catalyst amount caused a decline or marginal change in degradation efficiency. This behavior can be attributed to excessive catalyst loading, which leads to particle agglomeration around the active sites which reduces the production of reactive oxygen radicals that degrade the dye molecules [49]. A direct linear correlation was observed between catalyst amount and degradation efficiency prior to reaching the optimum value of 1 mg of ternary photocatalyst (as shown in Fig. 5b). Consequently, the optimum catalyst dosage was determined to be 1 mg of ternary CeO_2–$MnSe_2$–PANI nanocomposite.

3.4.2 Effect of dye concentration

The relationship between methylene blue (MB) concentration and photocatalytic degradation efficiency of the CeO_2–$MnSe_2$–PANI photocatalyst was investigated systematically by varying the initial dye concentration. The photocatalytic degradation was performed under sunlight irradiation where the initial MB dye concentration was varied between 40 ppm and 70 ppm at pH 8 with a fixed 20 mg of catalyst dosage. A clear inverse relationship was observed between degradation efficiency of ternary photocatalyst and MB dye concentration (as shown in Fig. 5a). The highest photocatalytic removal of 99.85% was achieved at 40 ppm concentration of MB dye and dropped to 97.61%, 92.36%, and 86.14% as the dye concentration was raised to 50, 60, and 70 ppm respectively. At lower MB concentrations, higher photocatalytic degradation was achieved due to the relatively smaller number of dye molecules present in the reaction system, which allowed more efficient interaction between the dye molecules and the photogenerated reactive species [50]. In addition, lower dye concentration reduced the blocking (absorption and scattering) of incoming light by the solution, allowing more photons to reach the catalyst surface. This type of unhindered light penetration boosts the formation of reactive oxygen species responsible for dye degradation. Conversely, in case of higher MB dye concentrations, the photocatalyst-dye solution becomes concentrated which leads to excessive dye molecules accumulation on the photocatalyst surface due to which the interaction between photons and photocatalyst is reduced and results in minimum degradation efficiency [51,52]. These findings suggest the existence of an optimal dye concentration value at which the photocatalyst exhibits the highest dye removal efficiency, attributed to the effective availability of active sites that promote efficient photon–catalyst interactions.

3.4.3 Effect of pH

A photocatalytic system is highly dependent on the pH of the dye-catalyst solution, which influences the photocatalyst surface charge, the ionisation behaviour of the dye molecules, the

dye-photocatalyst reactions, and the formation of reactive oxygen species [53]. In addition, changes in pH can influence the charge-transfer mechanism, band-edge positions, and overall surface-active sites, all of which directly affect photocatalytic performance. The effect of pH on the photocatalytic behavior of the synthesized CeO_2–$MnSe_2$–PANI photocatalyst under natural sunlight irradiation was assessed by adjusting the pH values between 6 and 9 of the dye-catalyst solution. The results indicate that the photodegradation of methylene blue (MB) strongly depends on solution pH. Owing to the cationic nature of the MB dye, its adsorption on the catalyst surface is increased in alkaline media. Under these conditions, the photocatalyst surface becomes negatively charged, generating an electrostatic pull that actively attracts the positively charged MB molecules [54]. Consequently, the ternary photocatalyst attained its peak photocatalytic removal efficiency of 99.85% at an optimum pH of 8, as shown in Fig. 5c. This improved degradation performance at pH = 8 can be attributed to the greater availability of hydroxyl ions (OH^-) in the alkaline media, which facilitates the formation of highly reactive $^{\bullet}OH$ radicals that are crucial for effective dye degradation. At lower pH values, a reduction in photocatalytic activity was observed, with degradation efficiencies of 90.99% at pH = 6 and 97.57% at pH = 7. This decrease is mainly due to electrostatic repulsion between the positively charged catalyst surface and MB molecules under acidic conditions, which limits dye adsorption and suppresses photocatalytic reactions. Similarly, a slight decline in degradation efficiency to 95.98% at pH = 9 was observed when the pH was increased beyond the optimum value. This type of photocatalytic behavior at higher pH can be ascribed to the reduced generation or scavenging of hydroxyl radicals by the abundant hydroxyl ions at higher alkalinity [55]. Overall, the results indicate that pH = 8 is the optimal condition for the degradation of MB dye using ternary CeO_2-$MnSe_2$-PANI photocatalyst but any up or down variation in pH value from the optimum value results in the decrease in photodegradation efficiency.

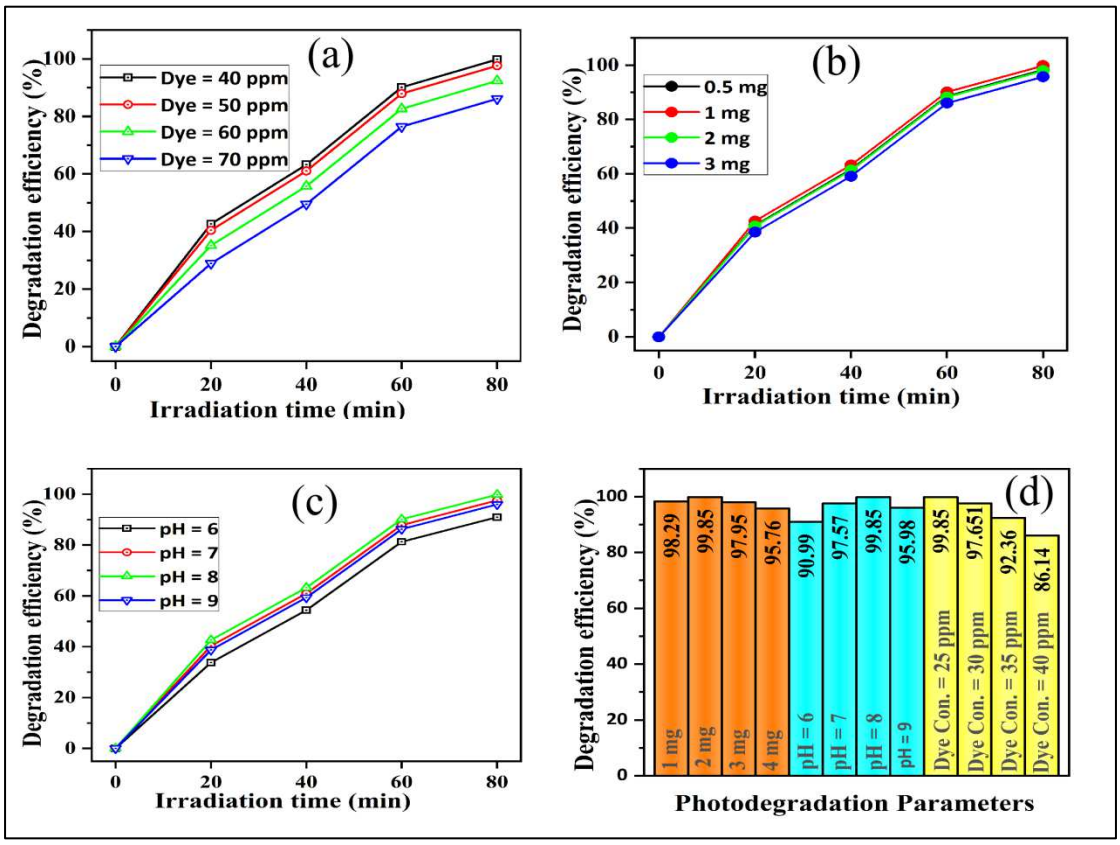


Fig. 5. Photodegradation efficiency of CeO_2-$MnSe_2$-PANI against MB dye under sunlight irradiation; (a) photocatalytic performance at different concentrations, (b) varying catalyst dosage, (c) effect of initial pH, and (d) photodegradation efficiency after 90 minutes across different varying parameters.

3.5. Free Radical Trapping Experiments

In the photodegradation process, the decomposition of organic dye pollutants is primarily driven by key reactive species generated during photocatalysis, such as hydroxyl (•OH) and superoxide ($•O_2^-$) radicals alongside photogenerated holes and electrons (h^+/e^-) [56]. Radical trapping experiments were performed to determine the primary dominant species driving the photocatalytic breakdown of methylene blue (MB). The reaction conditions were maintained under natural sunlight irradiation using a 40 ppm MB dye solution, catalyst loading of 20 mg, and a pH of 8. Different radical scavengers were employed to map out the possible reaction

mechanism and to elucidate the main active species involved in the photodegradation of methylene blue dye [57]. Both the photogenerated charge carriers (h^+/e^-) and their subsequent highly reactive free radical derivatives ($^{\bullet}OH$ and $^{\bullet}O_2^-$) were considered as the possible species for the photocatalytic degradation of methylene blue. For this purpose, specific scavengers such as isopropanol (10 mM), ASC (1 mM), EDTA-2Na (1 mM), and $AgNO_3$ (1 mM) were used to trap $^{\bullet}OH$, $^{\bullet}O_2^-$, h^+ and e− respectively [58]. The photocatalytic degradation efficiency was monitored in the presence of each scavenger and compared with the control experiment having only photocatalyst-dye solution in the absence of scavenger. A significant drop in degradation efficiency following the addition of a particular scavenger indicates the dominant role of the corresponding reactive species. For MB, the addition of isopropanol, ASC, EDTA-2Na and $AgNO_3$ led to an obvious decline in the degradation rate facilitated by CeO_2–$MnSe_2$–PANI, which specifically decreased to 31%, 23%, 87%, and 78% respectively in 40 minutes under sunlight irradiation in the presence of ternary CeO_2–$MnSe_2$–PANI photocatalyst (as shown in Fig. 6a). The introduction of EDTA-2Na and $AgNO_3$ hardly resist the degradation efficiency of the photocatalysts, while the addition of isopropanol and ASC greatly reduces the degradation efficiency of the fabricated photocatalysts. Based on the experimental data, $^{\bullet}OH$ and $^{\bullet}O_2^-$ were the dominant active species for the photocatalytic breakdown of MB dye using polyaniline supported dual Z-scheme CeO_2–$MnSe_2$–PANI photocatalyst.

3.6. Recyclability Test

The photocatalyst reusability is a crucial factor for its practical and large scale industrial application. Accordingly, the stability and repeatability of the fabricated dual Z-scheme CeO_2–$MnSe_2$–PANI nanocomposite were validated through multiple use tests. Under sunlight exposure, the ternary photocatalyst was subjected to six consecutive cycles of photocatalytic degradation of methylene blue (MB) dye. Following each MB photodegradation cycle, the catalyst was collected by centrifugation, rinsed repeatedly with deionised water, dried, and

deployed for the next cycle. As illustrated in Fig. 6b, only a slight decline in degradation efficiency from 99.85% to 90.35% was observed after the 6th cycle, which can be ascribed to the partial catalyst loss during the washing and recovery processes. These results highlight its strong potential for sustainable and industrial photocatalytic applications.

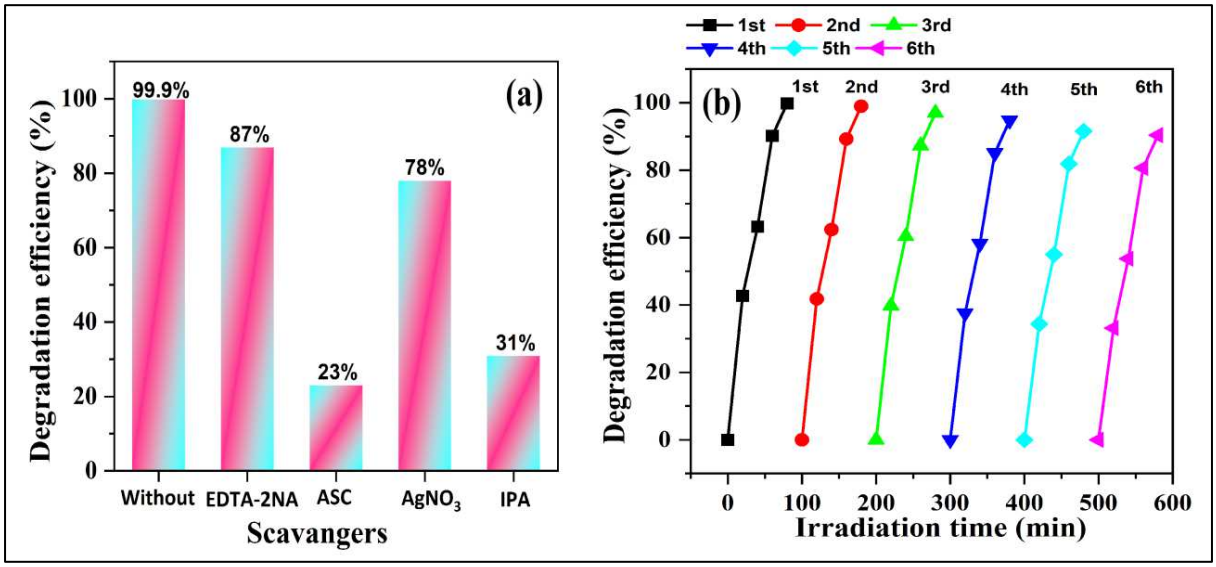


Fig. 6. MB degradation kinetics showing (a) the effects of various scavengers, and (b) catalyst stability over six consecutive degradation cycles.

3.7. Double Z-scheme Heterojunction Photocatalytic Mechanism of CeO_2-$MnSe_2$-PANI

A photocatalyst's performance is primarily determined by its light harvesting capacity, the excitation rate of photogenerated charge carriers, and rapid charge transfer between semi-conductors that minimize the recombination of charge carriers. Based on these features, two possible photocatalytic mechanisms of ternary CeO_2–$MnSe_2$–PANI have been designed against methylene blue (MB) dye (as shown in scheme-2). The initial phase of photocatalytic process involves the surface adsorption of MB dye molecules onto the active sites of CeO_2, $MnSe_2$, and the conductive PANI matrix. Upon solar light irradiation ($h\nu \geq E_g$), all three components are photoexcited, resulting in the generation of electron–hole (e^-/h^+) pairs. A fraction of these photogenerated charge carriers participate in surface redox reactions, while

others recombine rapidly. However, the intimate interfacial contact among CeO_2, $MnSe_2$, and PANI leads to the formation of a heterojunction, which significantly suppresses charge recombination and enhances photocatalytic efficiency. As expected, the visible-light absorption capability of the ternary nanocomposite was improved as compared to the individual semiconductors and the binary nanocomposite (as shown in Fig. 2a). Among them, CeO_2–$MnSe_2$–PANI demonstrates the most efficient visible-light harvesting, indicating its superior ability to make full use of solar radiation. A comprehensive understanding of the photocatalytic mechanism demands a prior analysis of the heterojunction interface established between the constituent nanomaterials. This includes mapping the conduction band (CB) and valence band (VB) positions of CeO_2, $MnSe_2$ and PANI, and production of reactive oxygen species (ROS). These factors govern the efficiency of any photocatalyst to separate and migrate photo-generated charge carriers due to which the reactive radical species are produced. The conduction band edge potential E_{CB} is calculated using the following empirical electronegativity equation [59]:

$$E_{CB} = X - E_e - 0.5E_g \quad (4)$$

$$E_{VB} = E_{CB} + E_g \quad (5)$$

Where X, E_e, E_g and are the absolute electronegativity, energy of free electrons (e^-) on the hydrogen scale, and the optical band gap energy (obtained from the Tauc plot) of the photocatalyst respectively.

The energy band positions of individual materials CeO_2, $MnSe_2$, and PANI are taken from published literature. For CeO_2, the CB and VB positions are located at -0.54 eV and +2.66 eV (E_g = 3.2 eV), whereas $MnSe_2$ displays band potentials of -0.82 eV and +1.18 eV (E_g = 2 eV) and PANI shows a VB of -1.9 eV and CB of +0.8 eV with an E_g value of 2.7 eV [60-62]. The oxidation and reduction potential values are -0.33 eV vs. NHE for $E(O2/^{\bullet}O_2^-)$, +1.99 eV vs. NHE for $E(OH^-/^{\bullet}OH)$ and +2.35 eV vs. NHE for $E(H_2O/^{\bullet}OH)$. On the basis of the above

discussion, we proposed two possible photocatalytic mechanisms of CeO_2–$MnSe_2$–PANI for MB dye degradation (as shown in scheme-2). For the first proposed mechanism, it was assumed that the ternary nanocomposite catalyst conformed to e^-/h^+ pair migration mechanism according to the type II conventional heterojunction. According to conventional heterojunction mechanism, the conduction band (CB) potentials of both $MnSe_2$ and PANI are located at more negative energies as compared to CB of CeO_2, whereas CeO_2 exhibits a valence band (VB) positioned at a more positive potential the valence band (VB) of CeO_2 is more positive than those of $MnSe_2$ and PANI. Upon sunlight irradiation, the electrons in CeO_2, $MnSe_2$ and PANI absorb light energy ($h\nu \geq Eg$) and produce photogenerated $e-/h^+$ pairs. The $e-$ produced in the conduction bands of $MnSe_2$ and PANI would migrate towards conduction band of CeO_2 while, at the same time h^+ produced in the valence band of CeO_2 would migrate to the valence bands of $MnSe_2$ and PANI to decrease their potentials. Following the charge carriers migration, the energetic position of the electrons in the conduction band of CeO_2 is more negative (-0.54 eV vs. NHE) than the standard reduction potential for superoxide anion radical formation (-0.33 eV vs. NHE). Thus, the surface adsorbed oxygen molecules undergoes reduction by the electrons accumulated in the conduction band of CeO_2 to generate superoxide anion radicals ($^{\bullet}O_2^-$) that break the structure of dye molecules and convert them into less harmful products (H_2O, CO_2 and corresponding mineral acids). Meanwhile, the photogenerated holes (h^+) accumulated in the valence bands of $MnSe_2$ (+1.18 eV vs. NHE) and PANI (+0.8 eV vs. NHE) possess insufficient potential to oxidize water or hydroxyl ions into hydroxyl radicals (+1.99 eV vs. NHE for $OH^-/^{\bullet}OH$ and +2.35 eV vs. NHE for $H_2O/^{\bullet}OH$). Thus, the holes in these valence bands are incapable of producing hydroxyl radicals to induce dye degradation. Therefore, according to type II conventional heterojunction, hydroxyl radicals ($^{\bullet}OH$) do not take part in the photodegradation process. Hence, this scheme of MB dye degradation is not advantageous, also it does not support the reactive ROS trapping experiments, in which both

527 $^{\bullet}O_2^-$ and $^{\bullet}OH$ were determined to be the dominant active species responsible for the
528 photocatalytic dye degradation.
529 According to the 2nd proposed mechanism involving a dual Z-scheme heterojunction, upon
530 irradiation of the ternary CeO_2–$MnSe_2$–PANI photocatalyst with sunlight, the electrons in
531 CeO_2, $MnSe_2$ and PANI absorb light energy ($h\nu \geq Eg$) and produce photogenerated e^-/h^+ pairs.
532 The e^- produced in the CB of CeO_2 would recombine with h^+ in the VBs of $MnSe_2$ and PANI;
533 thus, e^- in the CBs of $MnSe_2$/PANI and h^+ in the valence band of CeO_2 could be preserved,
534 promoting high charge carrier separation. In this case, the e^- in the conduction bands of both
535 $MnSe_2$ (-0.82 eV vs. NHE) and PANI (-1.9 eV vs. NHE) possess sufficient negative reduction
536 potentials to produce superoxide anion radicals (-0.33 eV vs. NHE). So, these accumulated e^-
537 interact with the absorbed oxygen molecules on the CeO_2–$MnSe_2$–PANI photocatalyst surface
538 and produce more superoxide anion radicals ($^{\bullet}O_2^-$). These highly reactive superoxide anion
539 radicals degrade the target dye molecules and convert them to less toxic substances. Similarly,
540 the valence band holes (h^+) of CeO_2 possess a highly positive potential (+2.64 eV vs. NHE) for
541 the generation of hydroxyl radicals via $OH^-/^{\bullet}OH$ (+1.99 eV vs. NHE) and $H_2O/^{\bullet}OH$ (+2.35 eV
542 vs. NHE). These hydroxyl radicals ($^{\bullet}OH$) subsequently attack the pollutant dye molecules,
543 resulting in their complete mineralization. Thus, the photodegradation mechanism in the dual
544 Z-scheme heterojunction involves the participation of both $^{\bullet}O_2^-$ and $^{\bullet}OH$ reactive species. It is
545 highly effective as compared to the type II conventional heterojunction in which only
546 superoxide radicals ($^{\bullet}OH$) take part in the photodegradation reaction. So, the dual z-scheme
547 heterojunction validates the results obtained from the free radical trapping experiment. The
548 charge transfer behaviour and corresponding reaction mechanisms for both scenarios are
549 illustrated below:

550 $$CeO_2 + h\nu \longrightarrow e^- (CeO_2) + h^+(CeO_2) \quad (6)$$

551 $$MnSe_2 + h\nu \longrightarrow e^-(MnSe_2) + h^+(MnSe_2) \quad (7)$$

$$PANI + h\nu \longrightarrow e^-(PANI) + h^+(PANI) \quad (8)$$

For type II conventional heterojunction:

$$e^- (CeO_2) + O_2 \longrightarrow \bullet O_2^- \quad (9)$$

$$\bullet O_2^- + \text{dye} \longrightarrow \text{Degradation Products} \quad (10)$$

$$h^+(MnSe_2, PANI) + OH^- \longrightarrow No\ Reaction$$

$$h^+(MnSe_2, PANI) + H_2O \longrightarrow No\ Reaction$$

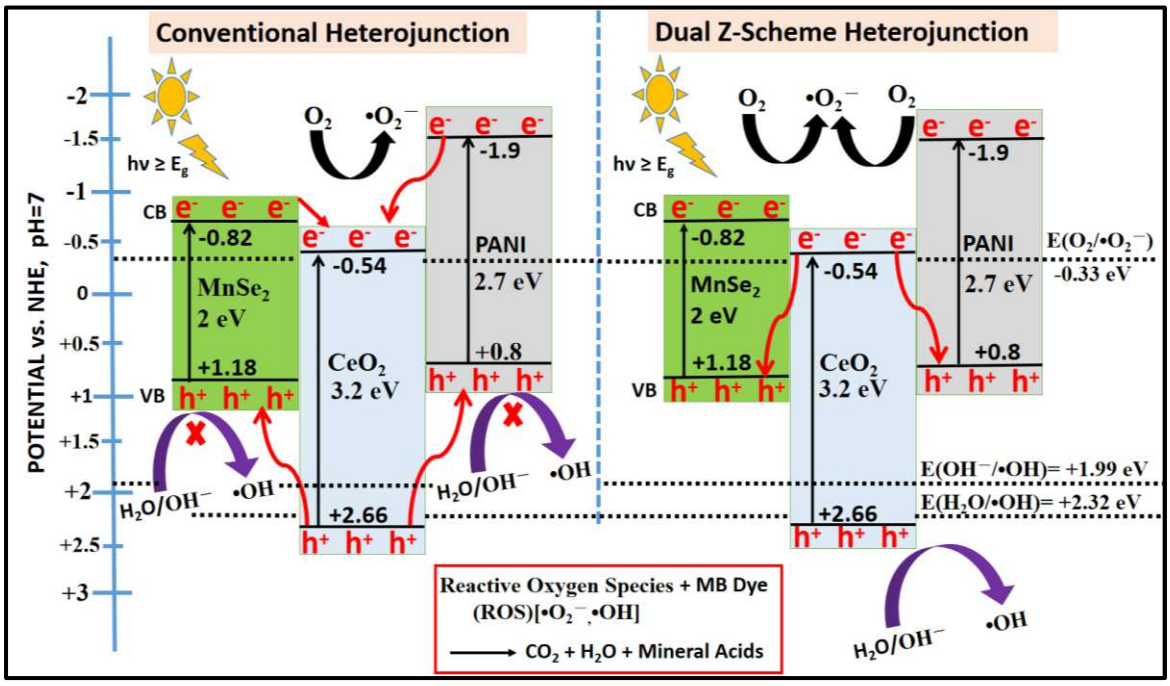
For Dual Z-Scheme Heterojunction:

$$e^-(MnSe_2, PANI) + O_2 \longrightarrow \bullet O_2^- \quad (11)$$

$$\bullet O_2^- + \text{dye} \longrightarrow \text{Degradation Products} \quad (12)$$

$$h^+(CeO_2) + OH^- \longrightarrow \bullet OH \quad (13) \qquad h^+(CeO_2) + H_2O \longrightarrow \bullet OH \quad (14)$$

$$\bullet OH + \text{dye} \longrightarrow \text{Degradation Products} \quad (15)$$



Scheme 2. Schematic illustration of photodegradation mechanism of CeO_2-$MnSe_2$-PANI nanocomposite.

4. Conclusion

In summary, a novel polyaniline supported dual Z-scheme heterostructure CeO_2-$MnSe_2$-PANI ternary nanocomposite photocatalyst was successfully prepared and characterized, demonstrating highly efficient photodegradation of methylene blue under sunlight irradiation. XRD analysis confirmed the phase purity and crystalline nature of CeO_2 and $MnSe_2$ within the nanocomposite, while TEM and HRTEM verified the intimate interfacial contact and successful formation of the CeO_2–$MnSe_2$–PANI heterostructure. UV-vis results showed the improved visible light-harvesting capability and a narrow band gap of 2.66 eV for the CeO_2–$MnSe_2$–PANI nanocomposite. The ternary photocatalyst demonstrated excellent photocatalytic performance towards MB dye degradation, achieving a maximum degradation efficiency of 99.85% with a high rate constant ($k = 0.074\ min^{-1}$), thereby significantly outperforming CeO_2, $MnSe_2$, and binary CeO_2–$MnSe_2$ nanocomposite. The peak photocatalytic performance was observed at the optimized conditions of 1 mg of catalyst dose, initial dye concentration of 40 ppm, and pH 8. The enhanced photocatalytic activity can be due to the effective integration of CeO_2, $MnSe_2$, and PANI in a single photocatalytic system. The identification of $^{\bullet}O_2^-$ and $^{\bullet}OH$ as the dominant active species for photodegradation of MB dye via radical scavenging tests provided clear evidence for dual Z-scheme heterojunction mechanism, which effectively reduced charge carriers recombination maintain elevated redox potential. The CeO_2–$MnSe_2$–PANI photocatalyst showed excellent photodegradation efficiency even after sixth consecutive degradation cycle with a slight decrease in efficiency. Therefore, the designed polyaniline supported dual Z-scheme heterostructure nanocomposite CeO_2–$MnSe_2$–PANI could be used as an efficient photocatalyst for sustainable water treatment applications.

Acknowledgement:

The authors express their gratitude to the department of Chemistry, University of Education, Vehari Campus, Vehari, Pakistan to provide all facilities to complete this manuscript.

Conflict of Interest:

None.

Data availability

The datasets used and/or analyzed during the current study available from the corresponding author on reasonable request.

Funding Declaration

There was no Funding received during this manuscript.

Author contributions

The specification of individual contribution of each author is as follows:

a. Nagina Naveed Riaz, Khalil Ahmad and Ahmad Hosseini Bandegharaei: Conceptualization, Data correction, Formal analysis, Investigation, Software, Project Administration, Resources, Validation, Visualization, Writing original draft, Writing-review & editing.

b. Muhammad Imran: Data correction, Formal analysis, Investigation, Resources, Software, Visualization, Writing original draft, Writing-review & editing.

c. Zuha Shahid: Data correction, Software, Validation, Visualization,

d. Eman Aldosari: Data correction, Software, Validation, Visualization.

e. Muhammad Mahboob Ahmad: Data correction, Formal analysis, Investigation, Software, Resources, Validation, Visualization, Writing original draft, Writing-review & editing.

References

1. Mukwevho, N.; Mabowa, M.H.; Bungani, T.; Toona, M.P.; Ntsasa, N.; Mkhoklakali, A.; Ncedo, T.; Chimuka, L.; Tshilongo, J.; Richards, H.; Letsoalo, M.R. Pollution assessment and apportionment of toxic elements within urban riverine: Economic implications for rehabilitation. Environ. Chall. 2025, 20, 101305.

2. Al-Tohamy, R.; Ali, S. S.; Li, F.; Okasha, K. M.; Mahmoud, Y. A. G.; Elsamahy, T.; Jiao, H.; Fu, Y.; Sun, J. A Critical Review on the Treatment of Dye-Containing Wastewater: Ecotoxicological and Health Concerns of Textile Dyes and Possible Remediation Approaches for Environmental Safety. Ecotoxicol. Environ. Saf. 2022, 231, 113160.

623 3. Saravanan, A.; Kumar, P. S.; Govarthanan, M.; George, C. S.; Vaishnavi, S.; Moulishwaran,
624 B.; Kumar, S. P.; Jeevanantham, S.; Yaashikaa, P. R. Adsorption Characteristics of Magnetic
625 Nanoparticles Coated Mixed Fungal Biomass for Toxic Cr(VI) Ions in Aquatic Environment.
626 Chemosphere 2021, 267, 129226.
627 4. Ma, D.; Yi, H.; Lai, C.; Liu, X.; Huo, X.; An, Z.; Li, L.; Fu, Y.; Li, B.; Zhang, M.; Qin, L.;
628 Liu, S.; Yang, L. Critical review of advanced oxidation processes in organic wastewater
629 treatment. Chemosphere 2021, 275, 130104.
630 5. Tong, H.; Ouyang, S.; Bi, Y.; Umezawa, N.; Oshikiri, M.; Ye, J. Nano-Photocatalytic
631 Materials: Possibilities and Challenges. Adv. Mater. 2012, 24, 229–251.
632 6. Poonia, K.; Patial, S.; Raizada, P.; Ahamad, T.; Aslam Parwaz Khan, A.; Le, Q. V.; Nguyen,
633 V-H.; Hussain, C. M.; Singh, P. Recent Advances in Metal Organic Framework (MOF)-Based
634 Hierarchical Composites for Water Treatment by Adsorptional Photocatalysis: A Review.
635 Environ. Res. 2023, 222, 115349.
636 7. Zango, Z. U.; Khoo, K. S.; Garba, A.; Kadir, H. A.; Usman, F.; Zango, M. U.; Oh, W. D.;
637 Lim, J. W. A Review on Superior Advanced Oxidation and Photocatalytic Degradation
638 Techniques for Perfluorooctanoic Acid (PFOA) Elimination from Wastewater. Environ. Res.
639 2023, 221, 115326.
640 8. Coccia, M.; Bontempi, E. New trajectories of technologies for the removal of pollutants and
641 emerging contaminants in the environment. Environ. Res. 2023, 229, 115938.
642 9. Lan, F.; Liu, C.S.; Zhou, C.; Huang, X.Z.; Wu, J.Y.; Zhang, X. Developing highly reducing
643 conjugated porous polymer: A metal-free and recyclable approach with superior performance
644 for pinacol C-C coupling under visible light. J. Mater. Chem. A 2022, 10, 16578–16584.
645 10. Puri, N.; Gupta, A. Water remediation using titanium and zinc oxide nanomaterials through
646 disinfection and photocatalysis process: A review. Environ. Res. 2023, 227, 115786.

11. Zhi, M.; Tang, H.; Wu, M.; Ouyang, C.; Zhang, Z.; Wu, N. Synthesis and Photocatalysis of Metal Oxide Aerogels: A Review. Energy & Fuels 2022, 36, 11359-11379.

12. Fauzi, A. A.; Jalil, A. A.; Hassan, N. S.; Aziz, F. F. A.; Azami, M. S.; Hussain, I.; Saravanan, R.; Vo, D. V. N. A critical review on relationship of CeO_2-based photocatalyst towards mechanistic degradation of organic pollutant. Chemosphere 2021, 286, 131651.

13. Ji, P.; Zhang, J.; Chen, F.; Anpo, M. Photoelectrochemical Properties of CeO_2 Nanocrystals: The Influence of Shape. J. Phys. Chem. C 2008, 112 (46), 17809–17813.

14. Yang, Z.-M.; Huang, G.-F.; Huang, W.-Q.; Wei, J.; Yan, X.-G.; Liu, Y.-Y.; Jiao, C.; Wan, Z.; Pan, A. Novel Ag_3PO_4/CeO_2 composite with high efficiency and stability for photocatalytic applications. J. Mater. Chem. A 2014, 2, 1750–1756.

15. Wen, X.-J.; Niu, C.-G.; Zhang, L.; Zeng, G.-M. Novel p–n heterojunction $BiOI/CeO_2$ photocatalyst for wider spectrum visible-light photocatalytic degradation of refractory pollutants. Dalton Trans., 2017, 46, 4982–4993.

16. Qu T, Yao X, Owens G, Gao L, Zhang H. Optimization and detailed stability study on Pb-doped ceria. Catalysis Today. 2021;506–513.

17. Rajappa V, Mohan S, Bharathkumar S, Rokhum SL, Fatehmulla A, Valdes H, Ilangovan R. Fe, N dual-doped cerium oxide photocatalyst manifesting the simultaneous degradation of dye–heavy metal mixed pollutants under sunlight. Industrial & Engineering Chemistry Research. 2024;63(50).

18. Yan H, Zhang N, Wang D. Highly efficient CeO_2-supported noble-metal catalysts: From single atoms to nanoclusters. Chem Catalysis. 2022;2(7):1594–1623.

19. Farouq M, Saleh A, Al-Ghamdi S, et al. Designing a novel highly efficient magnetic binary $NiFe_2O_4/CeO_2$ nano-photocatalyst for visible-light-driven degradation of organic pollutants. Applied Water Science. 2025;15:127.

671 20. Al-Essa K, Al-Essa E M, Qarqaz A, Al-Issa S, Alshahateet S F, Al-Fawares O. Graphitic
672 Carbon Nitride/CeO_2 Nanocomposite for Photocatalytic Degradation of Methyl Red. Water.
673 2025;17(2):158.
674 21. Hu S, Zhou F, Wang L, Zhang J. Preparation of Cu_2O/CeO_2 heterojunction photocatalyst
675 for the degradation of Acid Orange 7 under visible light irradiation. Catal.
676 Commun. 2011;12(9):794–797.
677 22. Yang Z, Huang G, Huang W, Wei J, Yan X, Liu Y, Jiao C, Wan Z, Pan A. Novel
678 Ag_3PO_4/CeO_2 composite with high efficiency and stability for photocatalytic applications. J.
679 Mater. Chem. A. 2014;2:1750–1756.
680 23. N. Wetchakun, S. Chaiwichain, B. Inceesungyorn, K. Pingmuang, S. Phanichphant, A. I.
681 Minett and J. Chen, ACS Appl. Mater. Interfaces, 2012, 4(7), 3718–3723.
682 24. Qiao Q, Pan A, Li C, Liu S, Wang Y, Tan H, Liang S. Facile in-situ construction of
683 mediator-free direct Z-scheme g-C_3N_4/CeO_2 heterojunctions with highly efficient
684 photocatalytic activity. J Phys D: Appl Phys. 2018;51(27):275302.
685 25. He S, Chi M, Gao H, Liu X, Wang T, Zhang L. Construction of core-shell heterojunction
686 regulating α-Fe_2O_3 layer on CeO_2 nanotube arrays enables highly efficient Z-scheme
687 photoelectrocatalysis. Appl Catal B: Environ. 2020;276:119138.
688 26. Zhou P, Yu J, Jaroniec M. All-solid-state Z-scheme photocatalytic systems. Adv Mater.
689 2014;26:4920–4935.
690 27. Ahmed, M. A.; Mohamed, A. A. Recent progress in semiconductor/graphene
691 photocatalysts: synthesis, photocatalytic applications, and challenges. RSC
692 Adv. 2023, 13, 421-439.
693 28. Chen, S.; Hisatomi, T.; Ma, G.; Wang, Z.; Pan, Z.; Takata, T.; Domen, K. Metal Selenides
694 for Photocatalytic Z-Scheme Pure Water Splitting Mediated by Reduced Graphene Oxide. Chin.
695 J. Catal. 2019, 40, 1668–1672.

29. Sobhani, A.; Salavati-Niasari, M. Transition Metal Selenides and Diselenides: Hydrothermal Fabrication, Investigation of Morphology, Particle Size and and Their Applications in Photocatalyst. Adv. Colloid Interface Sci. 2021, 287, 102321.

30. Hussain R A, Hussain I. Manganese selenide: synthetic aspects and applications. J Alloys Compd. 2020;842:155800.

31. Wang, J.; Lei, X.; Zhang, Y.; … S-Scheme Heterojunctions Formed by $MnSe_2$ Cubic Microparticles Supported on Red Phosphorus Nanosheets as Photocatalyst for H_2 Production. ACS Appl. Nano Mater. 2024, 7 (14), 16842–16851.

32. Jian, J.; Chen, H.; Xu, X.; Xie, Y.; Wei, S. Enhancement in wastewater refinement through a new cauliflower-like photocatalyst: $TiO_2/Bi_2MoO_6/MnSe_2$ heterojunction. Journal of Materials Science: Materials in Electronics 2023, 34, 2275.

33. Xie, M.; Zhang, T. A novel efficient visible-light-driven double Z-scheme PANI/Ag_3PO_4/CNO heterojunction photocatalyst mediated by PANI and in situ grown AgNPs. Journal of Materials Science 2020, 55, 3974–3990.

34. Kim, M.; Lee, C.; Jang, J. Fabrication of highly flexible, scalable, and high-performance supercapacitors using polyaniline/reduced graphene oxide film with enhanced electrical conductivity and crystallinity. Advanced Functional Materials 2014, 24, 2489–2499.

35. Wu, Q.; Xu, Y.; Yao, Z.; Liu, A.; Shi, G. Supercapacitors based on flexible graphene/polyaniline nanofiber composite films. *ACS Nano* 2010, 4, 1963–1970.

36. Jiang, W.; Luo, W.; Zong, R.; Yao, W.; Li, Z.; Zhu, Y. Polyaniline/carbon nitride nanosheets composite hydrogel: A separation-free and highly efficient photocatalyst with a 3D hierarchical structure. Small 2016, 12, 4370–4378.

37. Liu, L.; Ding, L.; Liu, Y.; An, W.; Lin, S.; Liang, Y.; Cui, W. A stable Ag_3PO_4@PANI core–shell hybrid: Enrichment photocatalytic degradation with π-π conjugation. Applied Catalysis B: Environmental 2017, 201, 92–104.

721 38. Bu, Y.; Chen, Z. Role of polyaniline on the photocatalytic degradation and stability
722 performance of the polyaniline/silver/silver phosphate composite under visible light. ACS
723 Applied Materials & Interfaces 2014, 6, 17589–17598.
724 39. Kumar, H.; Luthra, M.; Punia, M.; Singh, D. Ag2O@PANI nanocomposites for advanced
725 functional applications: A sustainable experimental and theoretical approach. Colloid Surf. A-
726 Physicochem. Eng. Asp. 2022, 640, 12.
727 40. X. Li, Z. L.; Fang, H.; Chen, Z. P.; Zou, W. X.; Zhao, C. X.; Yang, X. F. Regulating donor-
728 acceptor interactions in triazine-based conjugated polymers for boosted photocatalytic
729 hydrogen production. Applied Catalysis B: Environmental 2022, 312, 9
730 41. Yu, T.; Wang, D.; Li, L.; Song, W.; Pang, X.; Liang, C. A Novel Organic/Inorganic Dual
731 Z-Scheme Photocatalyst with Visible-Light Response for Organic Pollutants Degradation.
732 Catalysts 2023, 13(11), 1391.
733 42. Chen, F.; Wu, Y.; Ning, J.; Ren, J.; Zhang, Z.; Zheng, C.; Zhong, Y.; Hu, Y. Facile
734 preparation of ternary Ag_2CO_3/Ag/PANI composite nanorods with enhanced photoactivity and
735 stability. J. Mater. Sci. 2017, 52 (8), 4521–4531.
736 43. Guleria, A.; Sharma, R.; Singh, A.; Upadhyay, N. K.; Shandilya, P.; et al. Direct dual-Z-
737 scheme PANI/Ag_2O/Cu_2O heterojunction with broad absorption range for photocatalytic
738 degradation of methylene blue. J. Water Process Eng. 2021, 43, 102305.
739 44. Langhals, H.; Abbt-Braun, G.; Frimmel, F. Association of humic substances: verification
740 of Lambert–Beer law. Acta Hydrochim. Hydrobiol. 2000, 28(6), 329–332.
741 45. Mukhtar, F.; Munawar, T.; Nadeem, M. S.; Naveed ur Rehman, M.; Khan, S. A.; Koc, M.;
742 Batool, S.; Hasan, M.; Iqbal, F. Dual Z-scheme core-shell PANI-CeO_2-Fe_2O_3-NiO
743 heterostructured nanocomposite for dyes remediation under sunlight and bacterial disinfection.
744 *Environ. Res.* 2022, *215*, 114140.

745 46. Dhanalekshmi, S. B.; Priya, R.; Tamizh Selvi, K.; Alamelu Mangai, K.; Weldegebrieal, G.
746 K.; Garg, S.; Sagadevan, S. Microwave-assisted synthesis, characterization and photocatalytic
747 activity of mercury vanadate nanoparticles. *Inorg. Chem. Commun.* 2021, *131*, 108768.
748 47. Raha, S.; Ahmaruzzaman, M. Enhanced performance of a novel superparamagnetic g-
749 C_3N_4/NiO/ZnO/Fe_3O_4 nanohybrid photocatalyst for removal of esomeprazole: effects of
750 reaction parameters, co-existing substances and water matrices. *Chem. Eng. J.* 2020, 395,
751 124969.
752 48. Nasrollahzadeh, M. S.; Issaabadi, Z.; Sajjadi, M.; Atarod, M.; Varma, R. S. Synthesis of
753 ZnO nanostructure using activated carbon for photocatalytic degradation of methyl orange
754 from aqueous solutions. *Appl. Water Sci.* 2018, 8, 104.
755 49. Khan, I.; Saeed, K.; Khan, I. Heterogeneous photodegradation of industrial dyes: an insight
756 to different mechanisms and rate affecting parameters. *J. Environ. Chem. Eng.* 2020, 8(5),
757 104364.
758 50. Enesca, A.; Isac, L. The influence of light irradiation on the photocatalytic degradation of
759 organic pollutants. *Materials* 2020, 13, 2494.
760 51. Reza, K. M.; Kurny, A.; Gulshan, F. Parameters affecting the photocatalytic degradation
761 of dyes using TiO_2: a review. *Appl. Water Sci.* 2017, 7(4), 1569–1578.
762 52. Pandey, A.; Kalal, S.; Ameta, C.; Ameta, R.; Kumar, S.; Punjabi, P. B. Synthesis,
763 characterization and application of naïve and nano-sized titanium dioxide as a photocatalyst
764 for degradation of methylene blue. J. Saudi Chem. Soc. 2015, 19, 528–536.
765 53. Alkaim, A. F.; Aljeboree, A. M.; Alrazaq, N. A.; Baqir, S. J.; Hussein, F. H.; Lilo, A. J.
766 Effect of pH on adsorption and photocatalytic degradation efficiency of different catalysts on
767 removal of methylene blue. *Asian J. Chem.* 2014, 26, 8445–8448.

768 54. Azeez, F.; Al-Hetlani, E.; Arafa, M.; Abdelmonem, Y.; Nazeer, A. A.; Amin, M. O.;
769 Madkour, M. The effect of surface charge on photocatalytic degradation of methylene blue dye
770 using chargeable titania nanoparticles. *Sci. Rep.* 2018, 8, 7104.
771 55. Nuengmatcha, P.; Panthong, K.; Choi, J.; et al. Sonocatalytic performance of
772 ZnO/graphene/TiO_2 nanocomposite for degradation of dye pollutants (methylene blue,
773 Texbrite BAC-L, Texbrite BBU-L and Texbrite NFW-L) under ultrasonic irradiation. *Dyes*
774 *Pigm.* 2016, 134, 487–497.
775 56. Ngullie, R. C.; Alaswad, S. O.; Bhuvaneswari, K.; Shanmugam, P.; Pazhanivel, T.;
776 Arunachalam, P. Synthesis and characterization of efficient ZnO/g-C_3N_4 nanocomposites
777 photocatalyst for photocatalytic degradation of methylene blue. *Coatings* 2020, 10, 500.
778 57. Guo, Z.; Wang, G.; Fu, H.; Wang, P.; Liao, J.; Wang, A. Photocatalytic degradation of
779 methylene blue by a cocatalytic PDA/TiO_2 electrode produced by photoelectric polymerization.
780 *RSC Adv.* 2020, 10, 26133–26141.
781 58. Tabib, A.; Bouslama, W.; Sieber, B.; Addad, A.; Elhouichet, H.; Férid, M.; Boukherroub,
782 R. Structural and optical properties of Na-doped ZnO nanocrystals: Application to solar
783 photocatalysis. *Appl. Surf. Sci.* 2017, 396, 1528–1538.
784 59. Yan, H.; Wang, X.; Yao, M.; Yao, X. Band structure design of semiconductors for
785 enhanced photocatalytic activity: The case of TiO_2. Progress in Natural Science: Materials
786 International 2013, 23, 402–407.
787 60. Munawar, T.; Mukhtar, F.; Nadeem, M. S.; Manzoor, S.; Ashiq, M. N.; Mahmood, K.;
788 Batool, S.; Hasan, M.; Iqbal, F. Fabrication of dual Z-scheme TiO_2-WO_3-CeO_2 heterostructured
789 nanocomposite with enhanced photocatalysis, antibacterial, and electrochemical performance.
790 Journal of Alloys and Compounds 2022, 898, 162779.

791 61. Ghaly, H. A.; El-Kalliny, A. S.; Gad-Allah, T. A.; Abd El-Sattar, N. E. A.; Souaya, E. R.
792 Stable plasmonic Ag/AgCl–polyaniline photoactive composite for degradation of organic
793 contaminants under solar light. RSC Advances 2017, 7, 12726–12736.